Cite this as: https://dx.doi.org/10.1021/acsami.0c13166
ACS Appl. Mater. Interfaces 2020, 12, 44499−44507

# Dopamine Sensing Based on Ultrathin Fluorescent Metal−Organic Nanosheets

Faezeh Moghzi, Janet Soleimannejad,* Eva Carolina Sañudo, and Jan Janczak

ABSTRACT: The importance of dopamine (DA) detection as a biomarker for several diseases, especially Parkinson"s disease, has persuaded scientists to develop new nanomaterials for efficient sensing of DA in clinical samples. Ultrathin metal−organic nanosheets due to their exceptional thickness, large surface area, and flexibility are endowed with many accessible active sites and optimal surface interaction with the target analyte molecules. In this regard, a novel layered fluorescent metal−organic nanomaterial with a honeycomb topology based on europium, $[Eu(pzdc)(Hpzdc)(H_2O)]_n$ (ECP) ($H_2pzdc$ = 2,3-pyrazine dicarboxylic acid), was synthesized. X-ray crystallography revealed that the 3D supramolecular architecture of ECP is constructed from noncovalent interactions of coordinated water molecules between the 2D layers along the *b* axis. These layers that are only ~4 nm thick were conveniently separated through ultrasound-induced liquid phase exfoliation. Optical studies show that the reduction of ECP thickness enhances the fluorescence intensity and serves as an efficient optical marker for DA detection. ECP nanoflakes exhibited fast response and high selectivity for DA detection in clinical samples. Good linearity for DA detection in the range of 0.1−10 μM with a detection limit of 21 nM proves the potential of ECP

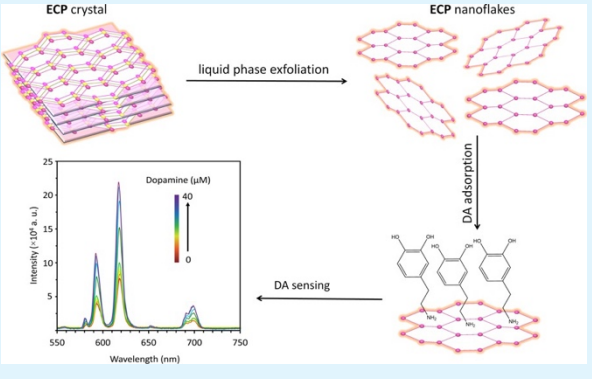


## 1. INTRODUCTION

Dopamine (DA) is a member of the catecholamine family and plays several vital roles in the brain and human body, especially in the neural system.[1] In the brain, DA functions as a neurotransmitter to send signals to nerve cells.[1] Abnormal levels of DA could be considered as an indication for many diseases such as cancer, Parkinson's, Schizophrenia, epilepsy, and memory loss.[2−4] Therefore, the selective and sensitive detection of DA is critical for the diagnosis of these diseases. The normal concentration of DA in urine and blood serum is 0.1 μM and in the cerebrospinal fluid it ranges from 0.5 to 25 nM.[5]

Diverse methodologies such as high-performance liquid chromatography, immunoassays, and spectrophotometry have been utilized for DA detection.[6−9] The limitations of such methodologies are intricate instrumentation, multitude of the process steps, complicated sample preparation, and time consumption.[10] Considering such limitations, electrochemical and optical methods have been developed as alternative methodologies for DA sensing in human serum, urine, and neuronal cell lines.[11−19] Despite their advantages for DA detection, electrochemical methods suffer from interfacial effects of competing species especially ascorbic acid (AA) with a similar oxidation potential.[20] Fluorescence detection methodologies with high selectivity and sensitivity, fast response, cost efficiency, and instrumentation ease-of-use can cover weaknesses of other analytical methods.[20] Moreover, by developing nanomaterials, the latter has proven to be an efficient methodology for DA detection.[21−24]

Currently, ultrathin 2D nanomaterials with single or several atomic layers have attracted remarkable attention because of their widespread applications such as catalysis, electronics, magnetics, optics, medicine, and sensing owing to their nanoscale and tunable thickness, large specific surface area, strong quantum confinement, optical transparency, mechanical flexibility, and their extremely high number of exposed surface atoms and accessible active sites.[25−30] Following the enormous success of graphene as a multifaceted single-atomic nanomaterial, efforts have been devoted to developing new ultrathin 2D nanomaterials beyond graphene that could expand our engineering and design freedom.[31−33]

Received: July 26, 2020
Accepted: September 15, 2020
Published: September 15, 2020

Ultrathin metal−organic nanosheets, as a pioneering family of 2D hybrid materials, have emerged because of their tunable structure and functionality.[34−40] Metal−organic materials (MOMs) are a rapidly growing class of organic−inorganic hybrid materials, which are built through the interconnection of the organic bridge ligands and metal centers to construct engineered, versatile, and tunable structures with a wide range of applications.[41−43] In the past decade, MOMs have attracted great attention as a new class of fluorescent materials for sensing applications because of the bridge organic ligands, metal centers, the interactions between them, and also some host−guest supramolecular interactions that allow MOMs to emit or induce fluorescence.[44,45] A few pioneering studies have proven the significant potential of 2D metal−organic nanosheets as fluorescent sensors owing to their large specific surface area and accessible active sites, which guarantees the high sensitivity and rapid response required for sensing applications.[46−49]

Considering the abovementioned characteristics of ultrathin metal−organic nanosheets that prove their potential as next-generation nanosensors, herein we report a novel ultrathin fluorescent metal−organic nanosheet of europium, $[Eu(pzdc)(Hpzdc)(H_2O)]_n$ (ECP), with highly sensitive and selective DA detection capability. ECP nanosheets were obtained using top-down liquid exfoliation in the presence of ultrasound irradiation and were fully characterized. Structural details were determined using X-ray crystallography. The liquid exfoliation process was carried out with several solvents to control the morphology of the ECP nanoflakes. Different parameters for DA sensing and the performance of ECP nanoflakes in the real samples were investigated and optimized.

## 2. RESULT AND DISCUSSION

**2.1. Crystal Structure of $[Eu(pzdc)(Hpzdc)(H_2O)]_n$.** The 2D metal−organic framework of $[Eu(Hpzdc)(pzdc)(H_2O)_3]_n$ (ECP) with a special honeycomb topology was formed *via* the reaction of $Eu^{3+}$ ions and $H_2pzdc$ in ambient condition. The crystal structure of ECP was determined using X-ray crystallography. As presented in Table 1, ECP is crystallized in the orthorhombic centrosymmetric space group *Pbca*. The asymmetric unit contains one $Eu^{3+}$ ion, which is connected to the $Hpzdc^-$ and $pzdc^{2-}$ anionic ligands and three coordinated water molecules (Figure 1a). In the crystal lattice, each $Eu^{3+}$ ion is nine-coordinated through two N atoms from Hpzdc and pzdc and seven O atoms from four monodentate carboxylates and three water molecules, which is compatible with the tricapped-trigonal prismatic geometry (Figure 1b).

In the $EuO_7N_2$ polyhedron, the four Eu−O bonds (the average distance of 2.373 c5) linking to carboxylate groups are slightly shorter than the Eu−O bonds linking the water molecules (average distance of 2.464 c5), while the two Eu−N bonds linking to the *N*-pyrazine ring are significantly longer (average distance of 2.782 c5). Table S1 shows bonds lengths and angles surrounding the central ECP atom. As shown in Figure 1c, each Eu atom is connected to three other Eu atoms through four organic bridge ligands to produce 3-connecting units. In this regard, self-assembly of 3-connecting Eu nodes and linear linkers (Hpzdc and pzdc) form the 2D metal− organic layers with hexagonal compact (hcp) (Figure 2a,b).

In the supramolecular architecture of compound ECP (Figure 3f), the coordinated water molecules have a key role in building the 3D supramolecular network where 2D metal− organic layers are connected through the intermolecular

Table 1. Crystal Data and Structure Refinement Details of ECP

| Crystal data | |
|---|---|
| chemical formula | $C_{12}H_{11}EuN_4O_{11}$ |
| $M_r$ | 539.21 |
| crystal system, space group | orthorhombic, *Pbca* |
| temperature (K) | 100 |
| *a*, *b*, *c* (c5) | 7.8240 (5), 14.5884 (8), 27.506 (2) |
| *V* (c5$^3$) | 3139.5 (3) |
| *Z* | 8 |
| radiation type | Mo Kα |
| μ (mm$^{-1}$) | 4.07 |
| crystal size (mm) | 0.21 × 0.12 × 0.11 |
| $T_{min}$, $T_{max}$ | 0.927, 1.000 |
| no. of measured, independent, and observed [$I > 2\sigma(I)$] reflections | 31781, 5495, 3291 |
| $R_{int}$ | 0.115 |

| | |
|---|---|
| $(\sin \theta/\lambda)_{max}$ ($c5^{-1}$) | 0.763 |
| $R[F^2 > 2\sigma(F^2)]$, $wR(F^2)$, $S$ | 0.049, 0.079, 1.02 |
| no. of reflections | 5495 |
| no. of parameters | 256 |
| H-atom treatment | H-atom parameters constrained |
| $\Delta\rangle_{max}$, $\Delta\rangle_{min}$ (e $c5^{-3}$) | 2.29, −1.39 |

hydrogen bonds of O2W−H2WA···O12[ii], O2W−H2WB···O3[ii], O3W−H3WA···O2[iii], and O3W−H3WB···O13[iv] (sym- metry code as in Table S2) among uncoordinated carboxylate groups with coordinated water molecules. The details of H- bonding geometries are given in Table S2.

2.2. General Characterization. The comparison between the powder X-ray diffraction (PXRD) pattern of the synthesized compound ECP and the simulated pattern of ECP single crystals' XRD data confirms that the synthesized compound ECP is structurally identical to $[Eu(pzdc)(Hpzdc)\text{-}(H_2O)_3]_n$ and the result shows single-phase purity of ECP (Figure 3a,b). Moreover, the stability of ECP bulk crystals in a biological fluid was studied by treating ECP in PBS for 6 h and as exhibited in Figure 3c, the PXRD pattern of ECP after treating with PBS confirms its stability in the biological fluid. As shown in Figure 4a, the infrared spectrum of ECP shows the symmetric $\nu_{sym}(COO)$ and asymmetric $\nu_{as}(COO)$ vibrations of the carboxylate groups at 1442 and 1635 $cm^{-1}$, which proves the linking of pyrazine dicarboxylic acids to ECP centers. Furthermore, a broad band located in the 3000−3500 $cm^{-1}$ region is attributed to the O−H stretching vibration of coordinated water molecules.

The thermal stability of $[Eu(pzdc)(Hpzdc)(H_2O)_3]_n$ was investigated *via* thermal gravity analysis in the range of 20− 1000 °C. As exhibited in Figure 5, TGA and DTA curves have two weight-loss steps and ECP is stable up to 200 °C. The first step could be attributed to coordinated water molecules and the decomposition occurred between 200 and 500 °C with a weight loss of 69.7% (calc. 69.0%). The exothermic peaks at 422 and 472 °C in the DTA curves confirm the full decomposition of ECP.

2.3. Top-Down Exfoliation of ECP. The bulk crystals of ECP, suitable for exfoliation, were washed with distilled water and dried in air. After the exfoliation process and at different time intervals, the formation of nanoflakes was examined using the Tyndall effect and SEM analysis. SEM images show that by increasing exfoliation time to 30 min, well-shaped ECP

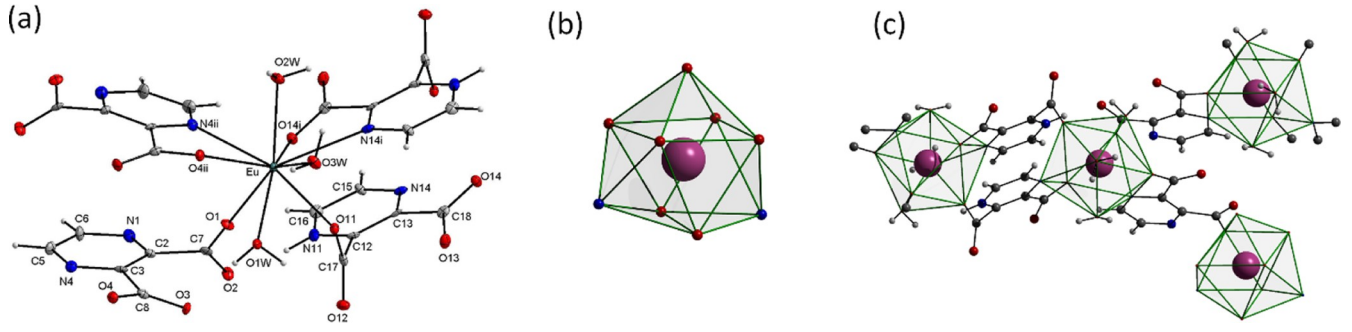


Figure 1. (a) Asymmetric unit and coordination environment of ECP with the atom numbering scheme (atoms with i and ii suffix are generated using (i) $-x + 1$, $-y + 1$, $-z + 1$ and (ii) $x + 1$, $y$, $z$ symmetry code), (b) coordination polyhedron of the ECP ion, and (c) coordination environment of Eu atom in ECP with regard to the pzdc bridging ligands.

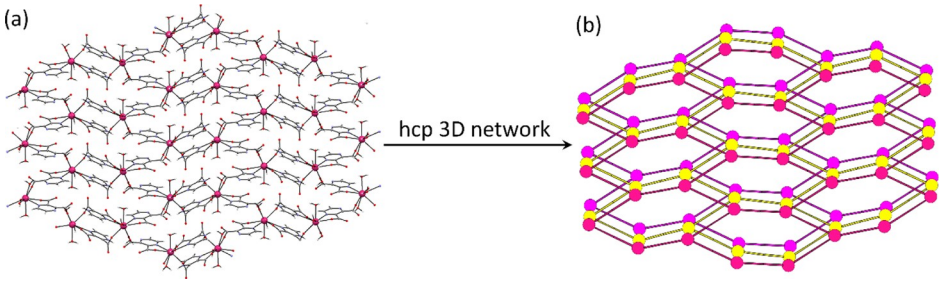


Figure 2. (a) 2D layer exhibition of ECP along the *ac* plane and (b) simplified exhibition of the 3D network with honeycomb topology.

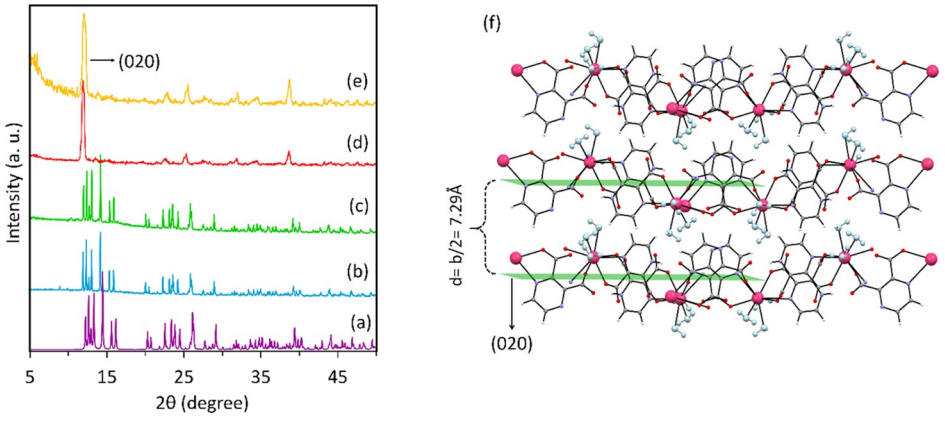


Figure 3. XRD patterns of the (a) simulated pattern based on single-crystal X-ray data of ECP, (b) bulk crystals of ECP prepared in ambient conditions, (c) bulk crystals of ECP treated by the PBS solution, (d) ECP nanoflakes formed through the LPE method, (e) ECP nanoflakes after DA adsorption, and (f) exhibition of 2D layers' orientation in the crystal lattice and packing of *ac* layers *via* noncovalent interactions between layers.

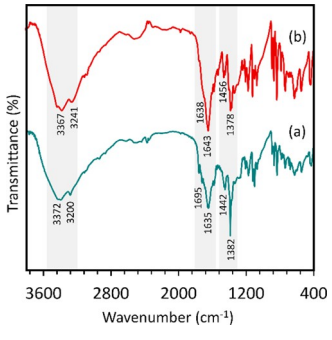


Figure 4. (a) IR spectra of ECP as the bulk crystal as synthesized and (b) IR spectra of ECP nanoflakes.

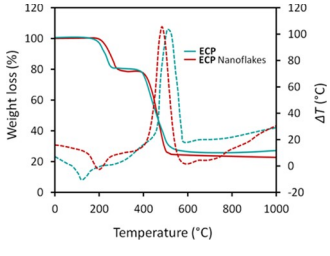


Figure 5. TGA and DTA of ECP: bulk crystals and synthesized *via* the LPE method.

nanosheets are formed and after 30 min the lateral size of the nanosheets is decreased. Therefore, 30 min was selected as an optimum duration for the delamination processes (Figure S1). The results confirm that all three solvents showed successful delamination of the layered crystal (Figures 6 and S1). As shown in Figure 6, the delamination in ethanol produces irregular nanosheets, in acetone the diamond-like nanosheets

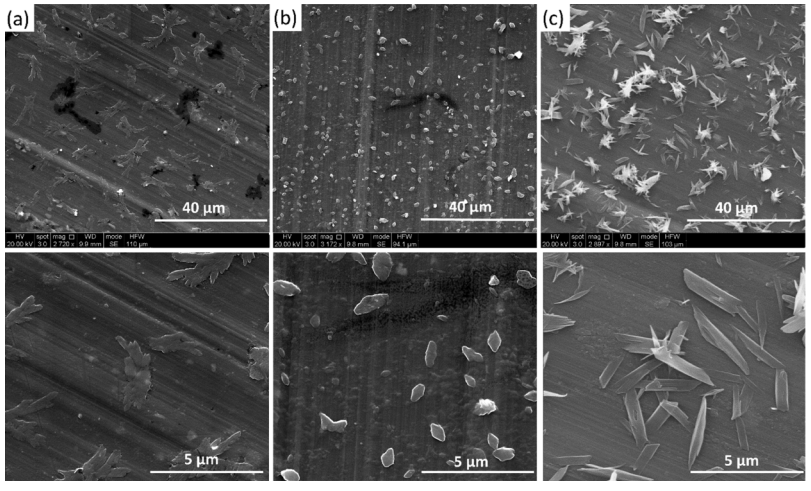


Figure 6. SEM micrographs of ECP nanoflakes prepared by the LPE method with different solvents: (a) ethanol, (b) acetone, and (c) distilled water.

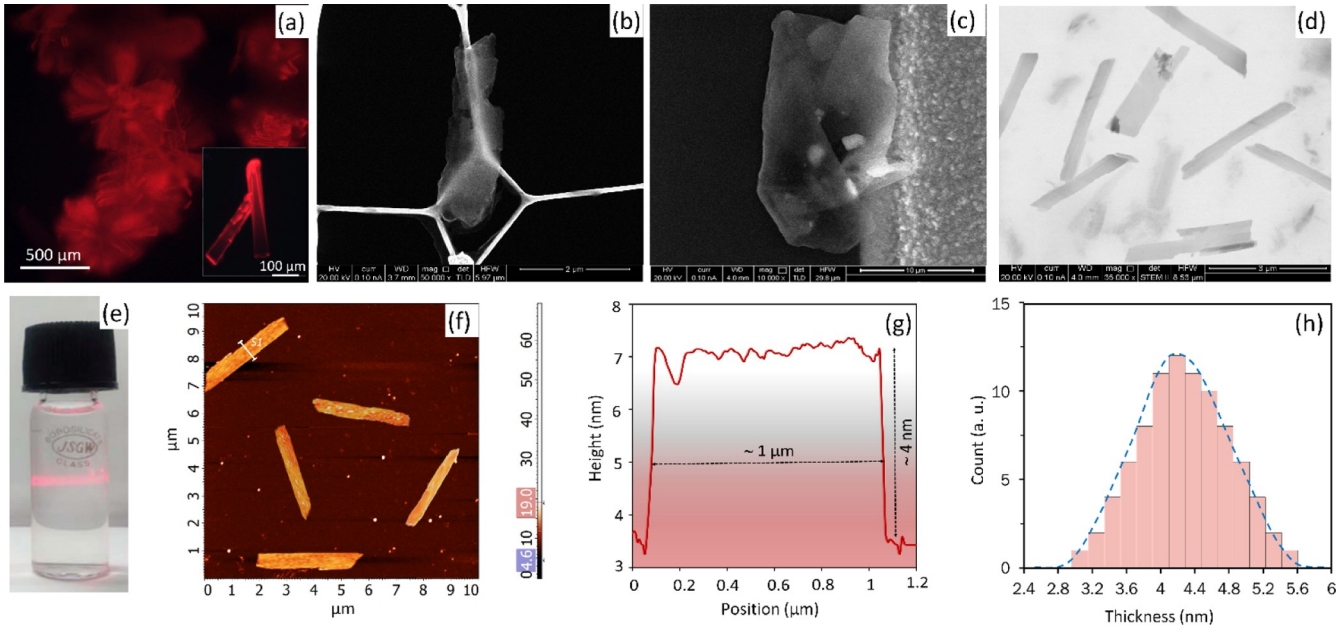


Figure 7. (a) Image of bulk crystal with red emission under the fluorescent microscope, (b−d) TEM images of ECP nanoflakes, (e) Tyndall effect demonstration of the colloidal suspension in water, (f) tapping mode AFM topography (in ambient air) of a layer on silicon substrate, (g) height profile corresponding to the line in (f), and (h) ECP nanosheets' thickness distributions as determined by AFM.

are formed, and the delamination process in distilled water results in the desired morphology with a higher yield than the other solvents. These results show the ability of the solvent to control the morphology of nanosheets and delamination in water keeps constant the morphology of the bulk crystals. Therefore, we selected distilled water as the proper solvent for the exfoliation and the prepared nanoflakes in water were used for further characterizations including PXRD, scanning transmission electron microscopy, Fourier transform infrared (FTIR), energy-dispersive X-ray, and atomic force microscopy (AFM).

As shown in Figure 7e the observation of the Tyndall effect confirms the formation of ECP nanoflake colloidal suspensions. Also, the PXRD pattern of ECP nanoflakes shows the formation of crystalline nanosheets with orientation in the direction of the *ac* plane (020), which confirms the exfoliation of the layered crystals because 2D networks are grown in *ac*

planes and hydrogen bonds have connected the 2D networks along the *b*-axis (Figure 3d,f). The results show that the noncovalent interactions between coordinated water molecules are broken with ultrasonic irradiation to form nanoflakes. As shown in Figure 4b, the FTIR spectra of ECP nanoflakes remained relatively constant after exfoliation, which suggests that only the noncovalent interactions are broken and coordinated water molecules are present in the network. Furthermore, the comparison between SEM and TEM of nanoflakes with an optical image of bulk crystals confirms that the morphology of crystals is kept constant (Figure 7b−d) during the exfoliation process and the nanoflakes are flexible. To specify the thickness of ECP nanoflakes, AFM was utilized. The thin films of ECP nanoflakes were prepared by deposition of nanoflakes onto the silicon substrate. AFM of the prepared thin films demonstrated ~4 nm average thickness and the results proved the formation of nanoflakes with ~6 atomic

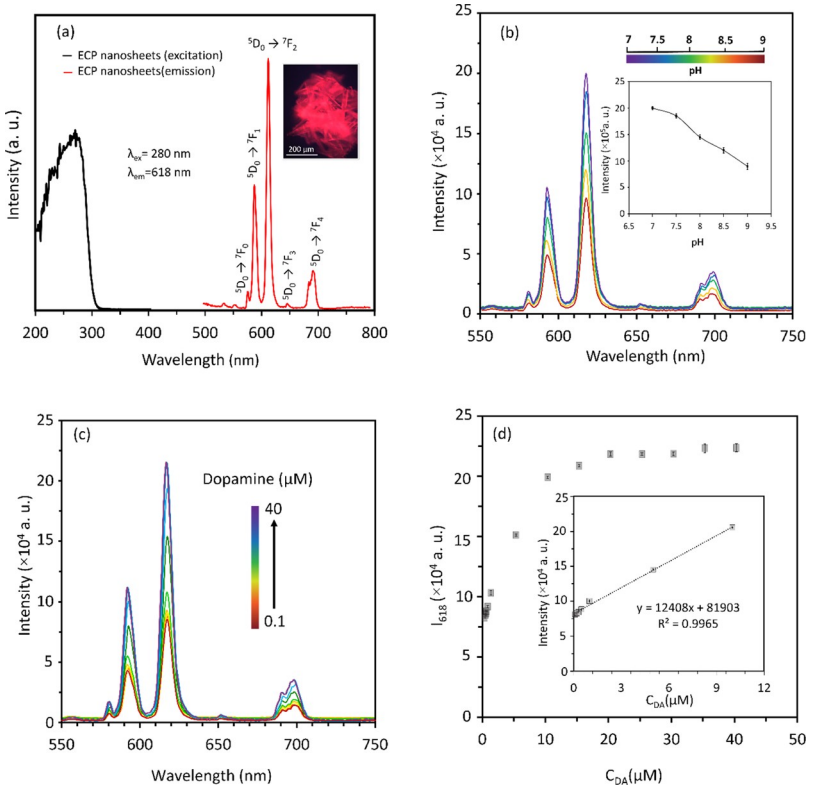


Figure 8. (a) Excitation and emission spectra of ECP bulk crystals. (b) Effect of pH on the emission intensity of ECP nanoflakes in the presence of DA (10 μM) in different pH conditions. (c) Fluorescence intensity of ECP nanoflakes in different DA concentrations and (d) plots of the ECP nanoflakes' emission at 618 nm vs DA concentration. Inset: The linear relationship between ECP nanoflakes' emission at 618 nm and DA concentration from 0.1 to 10 μM.

layers considering 0.729 nm *d*-space in the crystal lattice (Figures 3f, 7f−h). EDS mapping of ECP nanosheets is shown in Figure S2. The results of EDS confirm the stability of ECP after delamination.

*2.4.* Optical Properties and DA Detection. The performance of ECP nanoflakes for optical sensing was investigated based on the fluorescence intensity. To assess the optical properties of ECP, the absorption spectra of $H_2$pzdc and ECP were recorded from 200 to 700 nm in distilled water. As shown in Figures 8 and S3, both $H_2$pzdc and ECP show a broad absorption band with a maximum at 280 nm, which can be ascribed to the π → π* transition of the $H_2$pzdc organic ligand. The solid-state fluorescence of ECP upon a 280 nm excitation exhibited five characteristic $Eu^{3+}$ emission peaks at 581, 592, 618, 651, and 698 nm, attributed to the emission from the $^5D_0$ excited state of $Eu^{3+}$ ions to $^7F_j$ ($j$ = 0, 1, 2, 3, 4) states. The normalized absorption and emission spectra for ECP are shown in Figure 8a and the result proves the antenna effect of the $H_2$pzdc organic ligand for enhancing the emission of $Eu^{3+}$ ions. The comparison between the emission of ECP bulk crystals and nanoflakes (Figure S4) showed that the emission was enhanced upon reducing the vertical dimensions to several nanometers, which could be attributed to the scale-dependent internal electric field. The red emission with a maximum at 618 nm was used for DA sensing.[50]

To study the sensing capability of ECP nanoflakes for DA with the increase of the pH value from 7 to 9, the fluorescence intensities decreased. Considering the biological pH and maximum fluorescence intensity, we utilized the pH of 7.4 for further analyses. Also, the sensing time was monitored by recording the fluorescence intensity of ECP nanoflakes in the presence of DA and the results confirm a fast response where the fluorescence intensity reaches its maximum within 5 min (Figure S5). To assess the sensitivity of ECP nanoflakes for DA detection, we studied the fluorescence intensity of ECP nanoflakes in the presence of different DA concentrations, ranging from 0.1 to 40 μM (Figure 8c). Upon increasing the DA concentration from 0.1 to 10 μM, the fluorescence intensity of ECP nanoflakes was significantly enhanced but after 10 μM of DA concentration, the enhancement of fluorescence intensity was slow and the emission intensity was relatively constant above 20 μM of DA concentration. Interestingly, the change of fluorescence intensity against DA concentration showed a Langmuir adsorption behavior (Figure 8d), which is compatible with eq 1

$$\frac{1}{I - I_0} = \frac{1}{I_b - I_0} + \frac{1}{K(I_b - I_0)C_{DA}} \quad (1)$$

where $K$ is the association constant, $I_0$ is the emission intensity of ECP in the absence of DA, $I_b$ is the emission intensity of ECP with the excess amount of DA, $I$ is the fluorescence intensity of ECP in the presence of different amounts of DA, and $C_{DA}$ is the concentration of DA.[51] As shown in Figure S6,

sensing, the effects of pH and time on DA sensing were optimized in advance. The effect of pH on the emission intensity of ECP nanoflakes in the presence of DA (10 μM) was investigated at different pH values. As shown in Figure 8b,

DA

there is a linear relationship between $\frac{1}{I-I_0}$ and $\frac{1}{C_{DA}}$ from 0.1 to 10 μM of DA concentration, with a correlation coefficient ($R^2$) of 0.9972. The association constant was calculated from the

intercept/slope of the mentioned linear plot in Figure S4. The $K$ value $1.25 \times 10^5$ L mol$^{-1}$ confirms that DA is adsorbed on the surface of ECP nanoflakes and the association of DA is relatively strong. Furthermore, the fluorescence intensity has good linearity with DA concentration in the range 0.1−10 μm and is governed by the equation $y = 12408x + 81903$ with a correlation coefficient ($R^2$) of 0.9965 (Figure 8d inset). The limit of detection (LOD) was calculated according to the 3σ/s criterion, where σ is the standard deviation of blank measurements, b is the intercept, and s is the slope for the linear region of the fluorescence intensity against the DA concentration plot. LOD of ECP nanoflakes for DA sensing is 21 nM and this is lower than that of most reported nanomaterials (Table S3).

2.5. Selectivity and Reusability for DA Detection. To ensure the capability of ECP nanoflakes for DA detection in a practical sample, we examined the selectivity of ECP nanoflakes in the presence of the interfering species in biological samples including histidine (His), ascorbic acid (AA), uric acid (UA), citric acid (CA), arginine (AG), aspartic acid (Asp), alanine (AL), tyrosine (Tyr), glucose (G), $Na^+$, $K^+$, $Ca^{2+}$, $Mg^{2+}$, and $Zn^{2+}$. To study the effect of interfering species on fluorescence intensity of ECP nanoflakes, apart from individual sensing experiments for each of the species (50 μM) and DA (10 μM), a mixture of 10 μM of DA and 50 μM of each of the other interfering species including His, AA, CA, UA, AG, Asp, AL, Tyr, G, $Na^+$, $K^+$, $Ca^{2+}$, $Mg^{2+}$, and $Zn^{2+}$ was used and as shown in Figure 9, the interface effect of the other species is negligible, even when using fivefold higher concentrations of the interfering chemicals compared to DA.

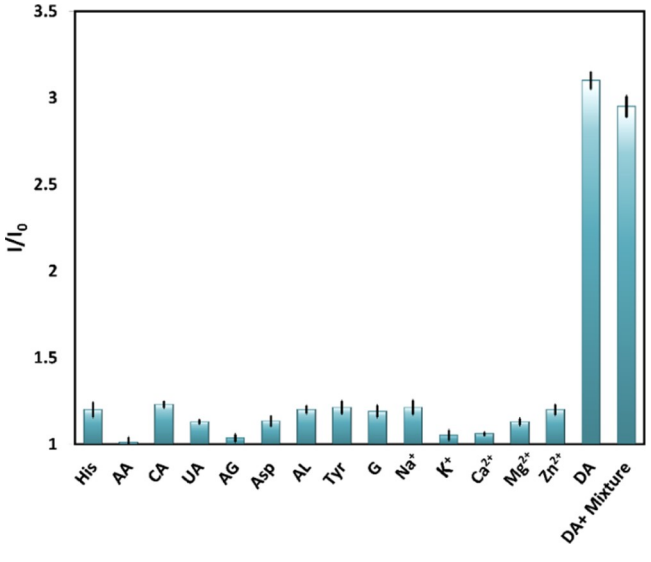


Figure 9. Sensing the selectivity of ECP nanoflakes in the presence of the interfering species in biological samples including histidine (His), ascorbic acid (AA), citric acid (CA) uric acid (UA), arginine (AG), aspartic acid (Asp), alanine (AL), tyrosine (Tyr), glucose (G), $Na^+$, $K^+$, $Ca^{2+}$, $Mg^{2+}$, and $Zn^{2+}$.

after DA adsorption is shown in Figure 3e and it confirms the stability of ECP nanosheets after DA adsorption. To investigate reusability, ECP nanosheets were immersed in distilled water for 1 day and then nanosheets were washed with water for five consecutive washes and were then used for DA detection. The results confirmed the reusability of ECP nanosheets and the efficiency of ECP nanosheets was only decreased by 4% after five cycles of DA adsorption and desorption (Figure S7).

2.6. Possible Mechanism of DA Detection. As mentioned before, the plot of fluorescence intensity of ECP nanoflakes against DA concentration is compatible with the Langmuir equation for isothermal adsorption and it confirms that DA molecules are adsorbed on the surface of the nanoflakes.[4,23,51] The PXRD of ECP nanoflakes after treating with the DA solution was measured and because this pattern remained relatively unchanged after adsorption, it can be concluded that ECP nanoflakes are stable after DA adsorption. To prove the adsorption of DA molecules on the surface of ECP nanoflakes, the zeta potential of pure ECP nanoflakes and the nanoflakes after DA exposure was investigated. The zeta potential value of ECP nanoflakes was −24 mV and after DA exposure, it changed to −17 mV. Changing the zeta potential values proves the electrostatic interaction between ECP nanoflakes and DA molecules.[51−54] Furthermore, the emission intensity of ECP nanoflakes in PBS solution due to the quenching effect of OH-oscillators decreased, but DA adsorption can recover the emission intensities of ECP nanoflakes. Therefore, DA-adsorbed molecules can protect ECP nanoflakes from the quenching effect of the environment. Furthermore, the absorption spectrum of DA shows a band with a maximum at 280 nm (Figure S3). Hence, it is possible that upon a 280 nm excitation, the adsorbed DA molecules transfer energy to ECP ions to enhance their emission and DA molecules show antenna effect for europium ions. To confirm the antenna effect of DA molecules for ECP nanoflakes, the luminescence decay of ECP nanoflakes before and after DA adsorption at the 280 nm excitation wavelength was studied. As shown in Figure S8, the lifetime of $Eu^{3+}$ fluorescence is increased after DA adsorption, which demonstrates energy transfer from DA molecules to ECP centers.[4,23,24,54]

2.7. DA Detection in Biological Samples. To prove the capability of ECP nanoflakes toward DA detection as a potential nanosensor, the performance of ECP nanoflakes in human serum samples was studied by the standard addition method. The human serum samples were diluted (100-fold) in a PBS buffer solution and the spiked samples were prepared by adding the DA solution. Then, the ECP nanoflakes were mixed in the samples and the fluorescence intensity of the mixtures was studied. As presented in Table 2, the quantitative recoveries for the fluorescence turn-on of DA detection were obtained between 90 and 99%. These results confirm the

Table 2. Results of the Luminescent Turn-On Detection of

DA in Biological Samples

These results confirm that ECP nanoflakes show high selectivity for DA adsorption and DA molecules can recover the fluorescence of ECP nanoflakes. Specially, we did not observe the interface effect of ascorbic acid, which is the main limitation of using electrochemical sensors for DA detection.

To prove the stability of ECP nanosheets for DA detection, they were examined by PXRD. The PXRD pattern of ECP

| sample | DA spiked (μM) | DA measured (mean ± std dev, μM) | recovery (mean ± std dev, %) |
|---|---|---|---|
| human serum | 1 | 0.98 ± 0.04 | 98 ± 4 |
| | 3 | 2.7 ± 0.13 | 90 ± 3 |
| | 5 | 4.71 ± 0.14 | 94 ± 3 |
| | 7 | 6.92 ± 0.10 | 99 ± 1 |

potential application of ECP nanoflakes for DA detection in clinical samples with acceptable recovery in comparison with other reported nanomaterials for DA detection (Table S3).

## 3. CONCLUSIONS

In summary, a novel 2D fluorescent metal−organic compound based on ECP was successfully synthesized in ambient conditions. The ECP supramolecular structure consists of 2D layers connected by a noncovalent interaction between coordinated solvents, which were simply cancelled upon ultrasound LPE. ECP nanoflakes demonstrated high selectivity and fast response features toward DA molecules in real samples, which serves as an efficient "turn-on" optical sensing mechanism for DA detection. Moreover, ECP nanoflakes show good linearity in the relevant DA detection range with very low LOD (21 nM) in comparison to other sensors, providing a new efficient method for DA detection. This simple method was utilized for DA detection in human serum and the results were in agreement with the results of the standard additions method with an acceptable recovery range. Although this marks a very early stage of research on ultrathin metal−organic nanosheets, the hybrid nature of the presented nanostructure and its graphene-like thickness, this class of nanomaterials opens up a brilliant future in many application areas, especially in biosensing.

## 4. EXPERIMENTAL SECTION

### 4.1. Synthesis of Single Crystal $[Eu(pzdc)(Hpzdc)(H_2O)]_n$.

*4.1.1. First Method.* The mixture of ligands including 2,3-pyrazine dicarboxylic acid (0.2 mmol, 34 mg) and piperazine (0.2 mmol, 18 mg) in 5 mL of distilled water was stirred for 5 min to solve them. The aqueous solution of $Eu(NO_3)_3 \cdot 5H_2O$ (2 mL)(0.1 mmol, 42 mg) was added to the mixture of ligands and stirred for 10 min in room temperature. Single crystals of $[Eu(Hpzdc)(pzdc)(H_2O)_3]_n$ (ECP) were grown for 1 day through slow evaporation with 87% yield, mp > 350 °C. Anal. Calcd for $C_{12}H_{11}EuN_4O_{11}$: C 26.7%, H 2.4%, N 10.9%. Found, C 26.9%, H 2.2%, N 10.7%, IR ($cm^{-1}$): 780 (s), 868 (s), 1117 (s), 1167 (s), 1361 (s), 1406 (s), 1456 (m), 1643 (vs), 3250 (m), 3370 (br).

*4.1.2. Second Method.* The method used here is exactly the same as the above procedure except that in this case piperazine was not used. Colorless block single crystals of ECP were obtained after 2 weeks through slow evaporation with 71% yield, mp > 350.

4.2. Exfoliation Process. ECP bulk crystals were exfoliated to 2D flakes with the liquid-solvent exfoliation (LPE) methodology assisted by an ultrasound probe tip. The effect of solvent upon the exfoliation process was investigated. The crystals (1 mg) were dispersed in 5 mL of diverse solvents including ethanol, acetone, and water. The dispersions were placed in a water-ice bath to avoid thermal decomposition of ECP and the ultrasound tip with 550 W power was immersed into dispersions for 10, 20, 30, 40, and 60 min. After sonication, the bulk crystals were collected in the bottom of the tube by centrifugation (1 min at 2000 rpm). At this stage, the nanoflakes remained suspended in the supernatant. To complete the delamination process, the suspension was kept under constant shaking condition for 12 h. A further centrifugation at 6000 rpm was carried out to separate unexfoliated crystals (which were lighter than the original bulk crystals). Finally, the solvent was evaporated with a rotary evaporator and nanoflakes were collected.

4.3. Detection of DA. To assay DA detection, the ECP nanoflakes (1 mg) were dispersed in a PBS buffer solution (2 mL, 0.1 M, pH 7.4) to form a stable suspension. A certain amount of DA was mixed with the above suspension, and the fluorescence spectra of ECP nanoflakes in the presence of DA were measured at different times at room temperature. The fluorescence intensities were measured at the excitation wavelength of 280 nm in the range of 350−800 nm using a quartz cuvette of 1 cm path length. To assess selectivity for DA detection, the fluorescence spectra were recorded in the presence of different interfacial species. To validate the experimental results, each measurement was repeated at least three times.

For DA sensing in the biological fluid, human serums were diluted 100 times using a PBS buffer solution. The standard solutions of DA, with different concentrations, were added to the diluted samples to prepare biological samples and 10 μL of these samples were mixed with a 2 mL suspension of the ECP nanoflakes (1 mg) in the PBS buffer solution (0.1 M, pH 7.4). After 5 min, the fluorescence spectra of samples were measured at room temperature.

## ASSOCIATED CONTENT

### Supporting Information

The Supporting Information is available free of charge at https://pubs.acs.org/doi/10.1021/acsami.0c13166.

Reagents and instruments, detailed crystal parameters of ECP, absorption spectra of 2,3-$H_2$pzdc ligand and DA, emission spectra of ECP nanoflakes, effect of pH on ECP nanoflakes, fluorescence spectra of ECP nanoflakes in the presence of DA at different points of time, and comparison of the performance of DA optical sensors in the previous and present studies (PDF)

## AUTHOR INFORMATION


### Corresponding Author

Janet Soleimannejad − *School of Chemistry, College of Science, University of Tehran, 6455 Tehran, Iran;* orcid.org/0000-0003-0327-5475; Email: janet_soleimannejad@

khayam.ut.ac.ir

## Authors

Faezeh Moghzi − *School of Chemistry, College of Science, University of Tehran, 6455 Tehran, Iran*

Eva Carolina Sañudo − *Departament de Química Inorgànica i Institut de Nanociència i Nanotecnologia, Universitat de Barcelona, 08028 Barcelona, Spain;* orcid.org/0000-0001- 9647-6406

Jan Janczak − *Institute of Low Temperature and Structure Research, Polish Academy of Science, 50950 Wrocław, Poland;* orcid.org/0000-0001-9826-5821

Complete contact information is available at: https://pubs.acs.org/10.1021/acsami.0c13166

## Notes

The authors declare no competing financial interest.

[CCDC 1940355 contains the supplementary crystallographic data for this paper. These data can be obtained free of charge from The Cambridge Crystallographic Data Centre *via* www.ccdc.cam.ac.uk/data_request/cif.]

## ACKNOWLEDGMENTS

This work was financially supported by the University of Tehran and the Spanish Government (grant no. PGC2018- 098630-B-I00).

## REFERENCES

(1) Tang, L.; Li, S.; Han, F.; Liu, L.; Xu, L.; Ma, W.; et al. SERS- active Au@Ag nanorod dimers for ultrasensitive dopamine detection. *Biosens. Bioelectron.* 2015, *71*, 7−12.

(2) Kriks, S.; Shim, J.-W.; Piao, J.; Ganat, Y. M.; Wakeman, D. R.; Xie, Z.; et al. Dopamine neurons derived from human ES cells efficiently engraft in animal models of Parkinson's disease. *Nature* 2011, *480*, 547−551.

(3) Li, B.-R.; Hsieh, Y.-J.; Chen, Y.-X.; Chung, Y.-T.; Pan, C.-Y.; Chen, Y.-T. An Ultrasensitive Nanowire-Transistor Biosensor for Detecting Dopamine Release from Living PC12 Cells under Hypoxic Stimulation. *J. Am. Chem. Soc.* 2013, *135*, 16034−16037.

(4) Ling, X.; Shi, R.; Zhang, J.; Liu, D.; Weng, M.; Zhang, C.; et al. Dual-Signal Luminescent Detection of Dopamine by a Single Type of Lanthanide-Doped Nanoparticles. *ACS Sens.* 2018, *3*, 1683−1689.

(5) Pathak, A.; Gupta, B. D. Ultra-selective fiber optic SPR platform for the sensing of dopamine in synthetic cerebrospinal fluid incorporating permselective nafion membrane and surface imprinted MWCNTs-PPy matrix. *Biosens. Bioelectron.* 2019, *133*, 205−214.

(6) Nichkova, M.; Wynveen, P. M.; Marc, D. T.; Huisman, H.; Kellermann, G. H. Validation of an ELISA for urinary dopamine: applications in monitoring treatment of dopamine-related disorders. *J. Neurochem.* 2013, *125*, 724−735.

(7) Syslová, K.; Rambousek, L.; Kuzma, M.; Najmanová, V.; Bubeníková-Valešová, V.; Šlamberová, R.; et al. Monitoring of dopamine and its metabolites in brain microdialysates: Method combining freeze-drying with liquid chromatography−tandem mass spectrometry. *J. Chromatogr. A* 2011, *1218*, 3382−3391.

(8) van Dongen, W. D.; Niessen, W. M. Bioanalytical LC−MS of therapeutic oligonucleotides. *Bioanalysis* 2011, *3*, 541−564.

(9) Mao, Y.; Bao, Y.; Gan, S.; Li, F.; Niu, L. Electrochemical sensor for dopamine based on a novel graphene-molecular imprinted polymers composite recognition element. *Biosens. Bioelectron.* 2011, *28*, 291−297.

(10) Ban, R.; Abdel-Halim, E. S.; Zhang, J.; Zhu, J.-J. β-Cyclodextrin functionalised gold nanoclusters as luminescence probes for the ultrasensitive detection of dopamine. *Analyst* 2015, *140*, 1046−1053.

(11) Li, H.; Yang, M.; Liu, J.; Zhang, Y.; Yang, Y.; Huang, H.; et al. A practical and highly sensitive C3N4-TYR fluorescent probe for convenient detection of dopamine. *Nanoscale* 2015, *7*, 12068−12075.

(12) Jeon, S.-J.; Kwak, S.-Y.; Yim, D.; Ju, J.-M.; Kim, J.-H. Chemically-Modulated Photoluminescence of Graphene Oxide for Selective Detection of Neurotransmitter by "Turn-On" Response. *J. Am. Chem. Soc.* 2014, *136*, 10842−10845.

(13) Silwal, A. P.; Yadav, R.; Sprague, J. E.; Lu, H. P. Raman Spectroscopic Signature Markers of Dopamine−Human Dopamine Transporter Interaction in Living Cells. *ACS Chem. Neurosci.* 2017, *8*, 1510−1518.

(14) Del Bonis-O'Donnell, J. T.; Thakrar, A.; Hirschberg, J. W.; Vong, D.; Queenan, B. N.; Fygenson, D. K.; et al. DNA-Stabilized Silver Nanoclusters as Specific, Ratiometric Fluorescent Dopamine Sensors. *ACS Chem. Neurosci.* 2018, *9*, 849−857.

(15) Emran, M. Y.; Shenashen, M. A.; Abdelwahab, A. A.; Khalifa, H.; Mekawy, M.; Akhtar, N.; Abdelmottaleb, M.; El-Safty, S. A. Design of hierarchical electrocatalytic mediator for one step, selective screening of biomolecules in biological fluid samples. *J. Appl. Electrochem.* 2018, *48*, 529−542.

(16) Emran, M. Y.; Shenashen, M. A.; Morita, H.; El-Safty, S. A. One-step selective screening of bioactive molecules in living cells using sulfur-doped microporous carbon. *Biosens. Bioelectron.* 2018, *109*, 237−245.

(17) Emran, M. Y.; Shenashen, M. A.; Mekawy, M.; Azzam, A. M.; Akhtar, N.; Gomaa, H.; Selim, M. M.; Faheem, A.; El-Safty, S. A. Ultrasensitive in-vitro monitoring of monoamine neurotransmitters-from dopaminergic cells. *Sens. Actuators, B* 2018, *259*, 114−124.

(18) Emran, M. Y.; Shenashen, M. A.; Abdelwahab, A. A.; Abdelmottaleb, M.; Khairy, M.; El-Safty, S. A. Nanohexagonal $Fe_2O_3$ Electrode for One-Step Selective Monitoring of Dopamine and Uric Acid in Biological Samples. *Electrocatalysis* 2018, *9*, 514−525.

(19) Emran, M. Y.; Shenashen, M. A.; Morita, H.; El-Safty, S. A. 3D-Ridge Stocked Layers of Nitrogen-Doped Mesoporous Carbon Nanosheets for Ultrasensitive Monitoring of Dopamine Released from PC12 Cells under $K^+$ Stimulation. *Adv. Healthcare Mater.* 2018, *7*, 1701459.

(20) Rasheed, P. A.; Lee, J.-S. Recent advances in optical detection of dopamine using nanomaterials. *Microchim. Acta* 2017, *184*, 1239− 1266.

(21) Lin, Y.; Yin, M.; Pu, F.; Ren, J.; Qu, X. DNA-Templated Silver Nanoparticles as a Platform for Highly Sensitive and Selective Fluorescence Turn-On Detection of Dopamine. *Small* 2011, *7*, 1557− 1561.

(22) Qian, C.-G.; Zhu, S.; Feng, P.-J.; Chen, Y.-L.; Yu, J.-C.; Tang, X.; et al. Conjugated Polymer Nanoparticles for Fluorescence Imaging and Sensing of Neurotransmitter Dopamine in Living Cells and the Brains of Zebrafish Larvae. *ACS Appl. Mater. Interfaces* 2015, *7*, 18581−18589.

(23) Chen, J.-L.; Yan, X.-P.; Meng, K.; Wang, S.-F. Graphene Oxide Based Photoinduced Charge Transfer Label-Free Near-Infrared Fluorescent Biosensor for Dopamine. *Anal. Chem.* 2011, *83*, 8787−
8793.

(24) Teng, Y.; Jia, X.; Li, J.; Wang, E. Ratiometric Fluorescence Detection of Tyrosinase Activity and Dopamine Using Thiolate- Protected Gold Nanoclusters. *Anal. Chem.* 2015, *87*, 4897−4902.

(25) Anichini, C.; Czepa, W.; Pakulski, D.; Aliprandi, A.; Ciesielski, A.; Samorì, P. Chemical sensing with 2D materials. *Chem. Soc. Rev.* 2018, *47*, 4860−4908.

(26) Sangwan, V. K.; Hersam, M. C. Electronic Transport in Two- Dimensional Materials. *Annu. Rev. Phys. Chem.* 2018, *69*, 299−325.

(27) Jin, H.; Guo, C.; Liu, X.; Liu, J.; Vasileff, A.; Jiao, Y.; et al. Emerging Two-Dimensional Nanomaterials for Electrocatalysis. *Chem. Rev.* 2018, *118*, 6337−6408.

*(28)* Zhang, H. Introduction: 2D Materials Chemistry. *Chem. Rev.* 2018, *118*, 6089−6090.

(29) Campuzano, S.; Pedrero, M.; Nikoleli, G.-P.; Pingarrón, J. M.; Nikolelis, D. P. Hybrid 2D-nanomaterials-based electrochemical immunosensing strategies for clinical biomarkers determination. *Biosens. Bioelectron.* 2017, *89*, 269−279.

(30) Zhu, C.; Du, D.; Lin, Y. Graphene-like 2D nanomaterial-based biointerfaces for biosensing applications. *Biosens. Bioelectron.* 2017, *89*, 43−55.

(31) Mas-Ballesté, R.; Gómez-Navarro, C.; Gómez-Herrero, J.; Zamora, F. 2D materials: To graphene and beyond. *Nanoscale* 2011, *3*, 20−30.

(32) C., Tan; X., Cao; X.-J., Wu; Q., He; J., Yang; X., Zhanget al., Recent Advances in Ultrathin Two-Dimensional Nanomaterials,
*Chem. Rev.*, *117*(2017). DOI: 10.1021/acs.chemrev.6b00558

(33) Zhang, H.; Cheng, H.-M.; Ye, P. 2D nanomaterials: beyond graphene and transition metal dichalcogenides. *Chem. Soc. Rev.* 2018, *47*, 6009−6012.

(34) Zhao, M.; Huang, Y.; Peng, Y.; Huang, Z.; Ma, Q.; Zhang, H. Two-dimensional metal−organic framework nanosheets: synthesis and applications. *Chem. Soc. Rev.* 2018, *47*, 6267−6295.

(35) Zhao, W.; Peng, J.; Wang, W.; Liu, S.; Zhao, Q.; Huang, W. Ultrathin two-dimensional metal-organic framework nanosheets for functional electronic devices. *Coord. Chem. Rev*. 2018, *377*, 44−63.

(36) Li, Y.-z.; Fu, Z.-h.; Xu, G. Metal-organic framework nanosheets: Preparation and applications. *Coord. Chem. Rev.* 2019, *388*, 79−106.

(37) Zhao, M.; Lu, Q.; Ma, Q.; Zhang, H. Two-Dimensional Metal−Organic Framework Nanosheets. *Small Methods* 2017, *1*, 1600030.

(38) Zhao, M.; Wang, Y.; Ma, Q.; Huang, Y.; Zhang, X.; Ping, J.; et al. Ultrathin 2D Metal−Organic Framework Nanosheets. *Adv. Mater.* 2015, *27*, 7372−7378.

(39) Zhu, W.; Yang, Y.; Jin, Q.; Chao, Y.; Tian, L.; Liu, J.; et al. Two-dimensional metal-organic-framework as a unique theranostic nano-platform for nuclear imaging and chemo-photodynamic cancer therapy. *Nano Res.* 2019, *12*, 1307−1312.

(40) Zhang, X.; Chang, L.; Yang, Z.; Shi, Y.; Long, C.; Han, J.; et al. Facile synthesis of ultrathin metal-organic framework nanosheets for Lewis acid catalysis. *Nano Res.* 2019, *12*, 437−440.

(41) Zhou, H.-C.; Long, J. R.; Yaghi, O. M. Introduction to Metal−Organic Frameworks. *Chem. Rev.* 2012, *112*, 673−674.

(42) Yuan, S.; Feng, L.; Wang, K.; Pang, J.; Bosch, M.; Lollar, C.; et al. Stable Metal−Organic Frameworks: Design, Synthesis, and Applications. *Adv. Mater.* 2018, *30*, 1704303.

(43) Safaei, M.; Foroughi, M. M.; Ebrahimpoor, N.; Jahani, S.; Omidi, A.; Khatami, M. A review on metal-organic frameworks: Synthesis and applications. *TrAC, Trends Anal. Chem.* 2019, *118*, 401−425.

(44) Cui, Y.; Yue, Y.; Qian, G.; Chen, B. Luminescent Functional Metal−Organic Frameworks. *Chem. Rev.* 2012, *112*, 1126−1162.

(45) Karmakar, A.; Samanta, P.; Desai, A. V.; Ghosh, S. K. Guest-Responsive Metal−Organic Frameworks as Scaffolds for Separation and Sensing Applications. *Acc. Chem. Res.* 2017, *50*, 2457−2469.

(46) Han, L.-J.; Zheng, D.; Chen, S.-G.; Zheng, H.-G.; Ma, J. A Highly Solvent-Stable Metal−Organic Framework Nanosheet: Morphology Control, Exfoliation, and Luminescent Property. *Small* 2018, *14*, 1703873.

(47) Maka, V. K.; Mukhopadhyay, A.; Savitha, G.; Moorthy, J. N. Fluorescent 2D metal−organic framework nanosheets (MONs): design, synthesis and sensing of explosive nitroaromatic compounds (NACs). *Nanoscale* 2018, *10*, 22389−22399.

(48) Xu, H.; Gao, J.; Qian, X.; Wang, J.; He, H.; Cui, Y.; et al. Metal−organic framework nanosheets for fast-response and highly sensitive luminescent sensing of Fe3+. *J. Mater. Chem. A* 2016, *4*, 10900−10905.

(49) Wong, B. J. C.; Xu, D.-M.; Bao, S.-S.; Zheng, L.-M.; Lei, J. Hofmann metal−organic framework monolayer nanosheets as an axial coordination platform for biosensing. *ACS Appl. Mater. Interfaces* 2019, *11*, 12986−12992.

(50) Li, Y.; Hu, R.; Zhang, X.; Yin, Z.; Qiu, J.; Yang, Z.; Song, Z. Emergence of photoluminescence enhancement of $Eu^{3+}$ doped BiOCl single-crystalline nanosheets at reduced vertical dimensions. *Nanoscale* 2018, *10*, 4865−4871.

(51) Li, P.; Ang, A. N.; Feng, H.; Li, S. F. Y. Rapid detection of an anthrax biomarker based on the recovered fluorescence of carbon dot−Cu(ii) systems. *J. Mater. Chem. C* 2017, *5*, 6962−6972.

(52) Cheng, Y.; Wu, J.; Guo, C.; Li, X.-G.; Ding, B.; Li, Y. A facile water-stable MOF-based "off on" fluorescent switch for label-free detection of dopamine in biological fluid. *J. Mater. Chem. B* 2017, *5*, 2524−2535.

(53) Ding, L.; Qin, Z.; Xiang, C.; Zhou, G. Novel Fluorescent Organic Nanoparticles as a Label-Free Biosensor for Dopamine in Serum. *J. Mater. Chem. B* 2017, *5*, 2750−2756.

(54) Tao, Y.; Lin, Y.; Ren, J.; Qu, X. A dual fluorometric and colorimetric sensor for dopamine based on BSA-stabilized Au nanoclusters. *Biosens. Bioelectron.* 2013, *42*, 41−46.